

# Implicit Active Shape Model Employing Boundary Classifier

Andreas Wimmer, Joachim Hornegger  
Chair of Pattern Recognition  
Friedrich-Alexander University Erlangen-Nuremberg,  
Erlangen, Germany  
Andreas.Wimmer@informatik.uni-erlangen.de

Grzegorz Soza  
Siemens Healthcare Sector  
Computed Tomography  
Forchheim, Germany  
Grzegorz.Soza@siemens.com

## Abstract

*We present an algorithm for the segmentation of the liver in 2-D computed tomography slice images. The basis for our algorithm is an implicit active shape model. In order to detect the liver boundary and guide the shape model deformation, a boundary classifier has been integrated into the implicit framework in a novel manner. The accuracy of the algorithm has been evaluated for 20 test cases including both normal and abnormal livers.*

## 1 Introduction

In perfusion computed tomography (CT) [6], the spread of contrast agent within an organ is monitored in a time series. This allows quantifying important diagnostic measures like blood flow and volume, alterations of which may for example indicate tumors or strokes. It is beneficial to have a segmentation of the organ, as one of the model inputs for perfusion imaging is the mean tissue time attenuation curve. In addition, segmentation could also form the basis when registering the time series in order to compensate for respiratory motions. Since even state of the art CT scanners are not capable of acquiring larger structures like the liver at high temporal resolution, perfusion CT is often limited to few slices which encompass the region of highest interest. Thus, we focus on 2-D segmentation of organ cross-sections in the following.

The remainder of this paper is organized as follows: in Sect. 2, related work is summarized. The proposed method is described in Sect. 3. Evaluation results are presented in Sect. 4, followed by a discussion and concluding remarks in Sect. 5.

## 2 Related work

Several approaches have been proposed for the segmentation of the liver in 2-D and 3-D datasets. Lim *et al* [4] obtain a 2-D segmentation by first performing a combination of thresholding and multi-scale morphological operations. The initial shape is then refined by searching for a smooth path in a gradient label map. Liu *et al* [5] employ a gradient vector flow (GVF) active contour for segmenting the liver. A Canny edge detector is used to generate an edge map, which is preprocessed in order to eliminate erroneously excluded concave regions prior to the GVF calculation.

A large number of interactive, semi-automatic, and fully automatic approaches for the 3-D segmentation of the liver competed in [2]. The most successfully automatic method was contributed by Kainmüller *et al* [3]. Like most other 3-D methods, it is based upon an active shape model (ASM) [1] of the liver. A heuristic intensity model is utilized for fitting the shape model to the image data.

## 3 Materials and methods

Segmenting organs in CT scans is a challenging task, as reduced radiation dose limits signal-to-noise ratio and contrast. Tissues belonging to different organs often are difficult to distinguish, for example at the boundary between liver and muscles surrounding the ribs.

Most 2-D liver segmentation methods base on some kind of active contour model. Heuristic approaches are usually incorporated to prevent the formation of inadmissible shapes, e.g. by removing concave regions, as mentioned above. This, however, limits their general applicability. In contrast, the majority of the 3-D methods employ active shape models. The increased robustness comes at the cost of a reduced flexibility of the model, which is usually relieved to some degree by allowing free-form deformations. When applying active

shape models for the 2-D segmentation of the liver, flexibility is of exceptional importance, since the model not only has to deal with the high inter subject variability of the liver but also has to address the inter slice variability. Clearly, segmenting the whole liver slice by slice using a single shape model is not feasible. However, as Sect. 4 will show, it is possible to segment slices acquired within a certain region using a shape model.

In this paper, the implicit active shape model of Rousson *et al* [8] has been chosen as basis. This model, reviewed in Sect. 3.1, features a traditional active contour constrained by an active shape model, providing for a robust yet flexible segmentation embedded in the level set framework [9]. Gray level appearance models are commonly used in explicit, i.e. landmark based, active shape models to guide the deforming model towards object boundaries of interest. The novel incorporation of such an appearance model into the implicit framework is described in Sect. 3.2

### 3.1 Implicit active shape model

The basis for the statistical shape model consists of a set of segmentation masks, which are obtained by manually segmenting the organ in reference data. In order to analyze shape variations, the first step is to eliminate variations due to similarity transformations, i.e. translation, rotation, and isotropic scaling. Therefore, one mask is chosen as reference and for the remaining masks, transformations are estimated which maximize the pair wise overlap between all training masks quantified by the alignment energy proposed by Tsai *et al* [10]. In 2-D, each transformation consists of a  $2 \times 2$  matrix accounting for scaling and in-plane rotation as well as a 2-D translation vector. The resulting 4 degrees of freedom per transformation are optimized through gradient descent. Since the method typically requires a large number of iterations and is prone to local minima, we first normalize translation, rotation, and scale (area) and then perform gradient descent from coarse to fine resolutions.

Following the alignment, the next step is to convert shapes encoded by the aligned masks into an implicit representation. This is accomplished by creating a signed distance map for each mask, whereby each grid point is assigned its positive or negative Euclidean distance to the boundary, depending on whether it is outside or inside the object.

Principal component analysis (PCA) is employed on the aligned signed distance maps in order to analyze the remaining variation, which is due to differences in

shape. New shapes are then expressed as

$$\psi(\boldsymbol{\lambda}) = \bar{\psi} + \sum_{i=1}^N \lambda_i \psi_i, \quad (1)$$

where  $\boldsymbol{\lambda}$  is the vector of mode weights  $\lambda_i$ ,  $\bar{\psi}$  is the average over all signed distance maps and  $\psi_i$  are the  $N$  significant Eigenmodes obtained from the PCA.

In order to employ the learnt model for image segmentation, another level set function  $\phi$  is introduced, which evolves as active contour according to the image content and which is constrained by the shape model. The fitting of active contour and shape model is formulated through the following energy functional, which measures the squared difference between both level set functions.

$$E(\psi, A, \boldsymbol{\lambda}) = \int_{\Omega} \delta(\phi) (\phi - \psi(A, \boldsymbol{\lambda}))^2 d\Omega \quad (2)$$

$A$  is an affine transform which aligns  $\psi$  with  $\phi$  and  $\boldsymbol{\lambda}$  again is the vector of mode weights. Since only the matching at the active contour, represented by the zero level set of  $\phi$ , is of interest, the Dirac delta function  $\delta$  is included in the above functional. The computational domain is denoted with  $\Omega \subset \mathbb{R}^2$ .

Equation (2) is minimized in an iterative manner by alternating optimization of  $\phi$  according to the calculus of variations of (2) on one hand, and of  $A$  and  $\boldsymbol{\lambda}$  by gradient descent on the other hand. We refer to [8] for further details. As mentioned above, the active contour level set function is evolved under both shape information and image information. The latter will be detailed in the following section.

### 3.2 Boundary classification based image term

In the context of explicit ASMs, appearance models are commonly used to guide the deformation [1]. This involves sampling intensities profiles at each landmark in surface normal direction during a training phase. Assuming a normal distribution, the appearance model is then obtained by calculating the mean and covariance matrix of the profiles. This principle has been extended to arbitrary distributions by sampling both boundary and non-boundary profiles and employing a nearest neighbor classifier [11]. During segmentation, each landmark point is moved in its normal direction towards the most probable boundary point. Compared to simple edge detectors, this approach greatly increases robustness.

In the following paragraph, we describe a novel integration of such an image term into implicit ASMs. The procedure is illustrated through Fig. 1. First, a narrow

band is created around the current zero level set of  $\phi$  using the Fast Marching algorithm [9]. For all grid points inside the narrow band, intensity profiles are sampled with the normal given by  $\nabla\phi$ . The probability of each point being part of the boundary is estimated through the appearance model. Compared to traditional explicit ASMs, where profiles are only sampled at landmarks, this approach is superior, especially in regions with high curvature. All boundary point candidates are then projected back onto the curve by gradient ascent (descent) on  $\phi$  for interior (exterior) boundary points until the zero level set is reached. Only the boundary point with the highest probability is kept along each path, all other candidates are discarded. Finally, for all pairs of interior and exterior paths ending at the same position of the zero level set, only the inside or outside boundary point is kept, depending on which one has the higher probability. The probability map is updated whenever the deforming contour reaches its boundary.

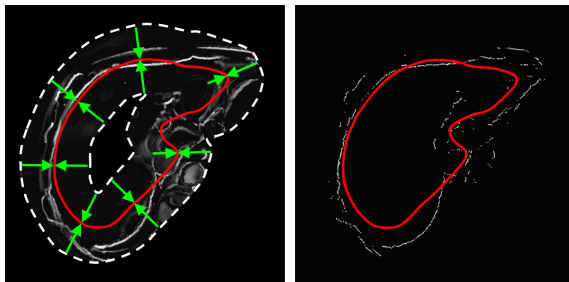


**Figure 1. Projection of probabilities. Left: boundary probabilities are calculated within the narrow band (dashed outline) and projected (arrows) onto the curve (solid line). Right: the point with the highest probability has been kept for each pair of interior/exterior projection paths.**

Since the capture range of such a probability map is limited, guiding the active contour towards boundary points solely using the gradient would not be sufficient. We therefore calculate the GVF of the probability image to diffuse the gradient vectors over the whole narrow band. This greatly increases the capture range. The GVF term is incorporated into the active contour evolution according to [7] and competes with the aforementioned shape constraint term imposed by (2). The evolution equation for the active contour level set function  $\phi$  is then

$$\frac{\partial}{\partial t}\phi = \alpha g |\nabla\phi| \operatorname{div} \left( \frac{\nabla\phi}{|\nabla\phi|} \right) - \beta g (\mathbf{v} \cdot \nabla\phi) - \gamma \delta(\phi) (\phi - \psi). \quad (3)$$

$g$  is a stopping function, “div” denotes the divergence operator, and  $\mathbf{v}$  is the GVF field. The first term on the right hand side of (3), weighted by  $\alpha$ , accounts for the smoothness of the curve. The second term, weighted by  $\beta$ , incorporates the GVF, driving the curve to boundary points. Finally, the third term, weighted by  $\gamma$ , constitutes the shape constraint and is derived from the calculus of variations of (2). We refer to [7] for more details on the first and second term, and to [8] for more details on the third term.

## 4 Evaluation

The proposed algorithm has been trained using 20 reference images and segmentations provided by a workshop on segmentation in the clinic [2]. Since this database consists of 3-D scans, all slices except for a single central slice with axial orientation were discarded beforehand. The central part is especially challenging since the liver separates there into the left and right lobe. In addition, several vessels are present in that region. All training and test images were acquired with varying levels of contrast enhancement and comprised both normal and abnormal livers exhibiting pathological alterations like tumors. All images had their histograms standardized with respect to a reference image prior to isotropic diffusion filtering. A  $k$  nearest neighbor classifier with  $k = 20$  was chosen as appearance model. The training set consisted of profiles with 7 samples at 2 mm spacing.

In order to evaluate the algorithm, 20 central slices from a different database were selected. The same pre-processing steps, i.e. histogram standardization and diffusion filtering, were applied. The segmentation was started with a grid of size  $128 \times 128$ . After convergence was reached on one level, calculations were performed at the next finer level with doubled resolution up to the original slice size of  $512 \times 512$ . The results of the segmentation algorithm were compared to manual segmentations. In order to evaluate accuracy, the area overlap ( $A_{OL}$ , %) and area difference ( $A_{\Delta}$ , relative w.r.t ref. segmentation) were calculated as well as the symmetric mean absolute ( $d_{abs}$ , mm), root mean squared ( $d_{rms}$ , mm), and maximum ( $d_{max}$ , mm) boundary distance. The results of these evaluation metrics are listed in Table 1. Images are shown in Fig. 2 for cases 2 and 3 (top row) and cases 7 and 9 (bottom row).

## 5 Discussion and conclusion

Table 1 shows the proposed algorithm is able to accurately segment the liver. For the majority of test cases,

**Table 1. Evaluation results for all test cases. From left to right: area overlap (%) and rel. difference, symmetric mean abs., root mean squared, and max. boundary distance (mm).**

| Case | $A_{OL}$ | $A_{\Delta}$ | $d_{abs}$ | $d_{rms}$ | $d_{max}$ |
|------|----------|--------------|-----------|-----------|-----------|
| 1    | 96.4     | 0.7          | 1.9       | 3.0       | 14.6      |
| 2    | 97.4     | -0.3         | 1.1       | 1.7       | 7.9       |
| 3    | 98.5     | -2.3         | 0.7       | 1.0       | 4.7       |
| 4    | 95.6     | 1.0          | 2.9       | 6.0       | 27.2      |
| 5    | 95.2     | -2.4         | 2.3       | 4.3       | 19.0      |
| 6    | 97.4     | -2.9         | 1.3       | 1.8       | 6.8       |
| 7    | 96.7     | -3.3         | 1.2       | 2.1       | 12.0      |
| 8    | 96.4     | 0.7          | 1.9       | 4.3       | 22.2      |
| 9    | 81.1     | -28.6        | 11.0      | 22.2      | 79.0      |
| 10   | 96.5     | -6.2         | 1.7       | 2.4       | 9.4       |
| 11   | 97.3     | -0.3         | 1.6       | 2.3       | 9.3       |
| 12   | 97.6     | -2.4         | 0.9       | 1.5       | 7.2       |
| 13   | 89.7     | -5.1         | 4.3       | 7.0       | 26.1      |
| 14   | 97.6     | -2.6         | 1.1       | 2.2       | 14.9      |
| 15   | 96.8     | -4.2         | 1.6       | 2.7       | 12.4      |
| 16   | 95.3     | -0.2         | 2.5       | 4.1       | 19.4      |
| 17   | 94.7     | -3.7         | 2.6       | 5.2       | 26.0      |
| 18   | 93.5     | -5.9         | 3.6       | 6.5       | 32.7      |
| 19   | 95.4     | -6.6         | 2.3       | 3.3       | 13.2      |
| 20   | 97.2     | -0.9         | 1.3       | 2.3       | 11.0      |

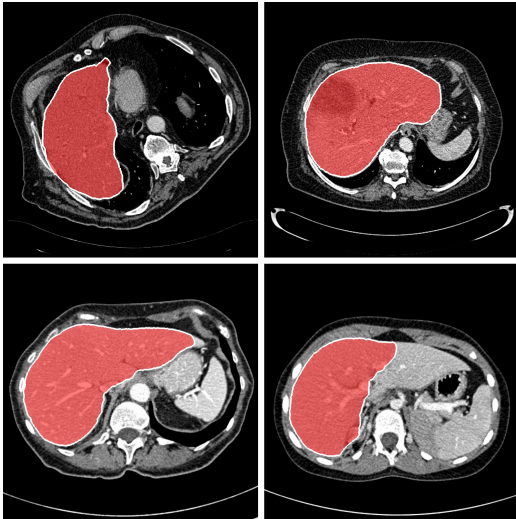


**Figure 2. Segmentation results for case 2 and 3 (top row) and case 7 and 9 (bottom row).**

the area overlap is larger than 95% while at the same time, the mean absolute surface distance is below or close to 2 mm. Large maximum boundary distances are mostly caused by deviations in the region of the vena cava. Undersegmentation occurred at the apex of elongated livers. The algorithm failed for case 9. Due to a bad initialization, the right part of the liver was entirely missed and the fitting only took place for the left part. For images with poor quality or pathologies (e.g. the tumor in case 3, see dark region in Fig. 2), the algorithm proved to be robust.

One possible direction of future research could be the inclusion of a region term besides the boundary term in order to obtain a more global solution. Furthermore, by utilizing individual appearance models for different regions, the quality of boundary detection might be increased.

## References

- [1] T. F. Cootes, D. Cooper, C. J. Taylor, and J. Graham. Active shape models – their training and application. *CVIU*, 61(1):38–59, 1995.
- [2] T. Heimann, M. Styner, and B. van Ginneken, editors. *3D Segmentation in the Clinic – A Grand Challenge*. MICCAI Workshop, 2007.
- [3] D. Kainmüller, T. Lange, and H. Lamecker. Shape constrained automatic segmentation of the liver based on a heuristic intensity model. In *3D Segmentation in the Clinic – A Grand Challenge*, pages 109–116, 2007.
- [4] S. J. Lim, Y. Y. Jeon, and Y. S. Ho. Segmentation of the liver using the deformable contour method on CT images. In *PCM*, volume 3767, pages 570–581, 2005.
- [5] F. Liu, B. Zhao, P. K. Kijewski, L. Wang, and L. H. Schwartz. Liver segmentation for CT images using GVF snake. *Medical Physics*, 32(12):3699–3706, 2005.
- [6] K. A. Miles and M. R. Griffith. Perfusion CT: a worthwhile enhancement? In *British Journal of Radiology*, volume 76, pages 220–231, 2003.
- [7] N. Paragios, O. Mellina-Gottardo, and V. Ramesh. Gradient vector flow fast geodesic active contours. In *ICCV*, pages 67–73, 2001.
- [8] M. Rousson, N. Paragios, and R. Deriche. Implicit active shape models for 3D segmentation in MR imaging. In *MICCAI LNCS*, volume 3216, pages 209–216, 2004.
- [9] J. A. Sethian. *Level Set Methods and Fast Marching Methods*. Cambridge University Press, New York, USA, 2nd edition, 1999.
- [10] A. Tsai, A. Yezzi, W. Wells, C. Tempany, and D. T. et al. A shape-based approach to the segmentation of medical imagery using level sets. *IEEE Transactions on Medical Imaging*, 22(2):137–154, 2003.
- [11] B. van Ginneken, A. F. Frangi, J. J. Staal, B. M. ter Haar Romeny, and M. A. Viergever. Active shape model segmentation with optimal features. *IEEE Transactions on Medical Imaging*, 21(8):924–933, 2002.